Granular Matter (2024) 26:34
https://doi.org/10.1007/s10035-024-01394-7

ORIGINAL REPORT

Plastic deformation effect on contact behaviour in granular materials

F. N. Altuhafi[1] · **B. A. Baudet**[1] · **M. R. Coop**[1]

Received: 28 September 2023 / Accepted: 31 December 2023 / Published online: 1 March 2024
© The Author(s) 2024

Abstract
Contact tests on machined and natural granite showed that extensive plastic deformation which extends to the core shape is happening before the cross-over from the behaviour of an elastic rough surface to the Hertzian behaviour of an elastic smooth contact when all asperities have yielded in the surface. The plastic deformation, which was found to take place when the estimated maximum stresses at the contact reaches about 0.6 of the material hardness, affects the behaviour during normal loading as the material will start to deform at constant stiffness after reaching these stresses. The plastic deformation during lateral loading also affects the applicability of lateral loading models. The data yielded a much lower lateral stiffness which is around one order of magnitude less than that predicted by the available contact models.

Keywords Contact mechanics · Ballast · Modelling · Contact stiffness

List of symbols

a_H	Radius of the circle delimiting the contact surface in Hertz model
a^*	Radius of area in contact for rough surfaces
A_0	Area of contact at full yielding of asperities
D_f	Fractal dimension
E^*	Combined modulus of elasticity of the two surfaces in contact
H_{st}	Hurst exponent
H_v	Vicker's Hardness number
k_N^H	Hertz normal stiffness
$K_N^{P\&P}$	Normal stiffness as predicted by Pohrt and Popov
K_N^{RMS}	Normal RMS stiffness
${}^*K_N^{RMS}$	Normalised RMS stiffness
K_T	Lateral stiffness
p_0	Maximum contact pressure
P	Normal load
R	Equivalent radius of curvature for the two surfaces in contact.
S_q	Root mean square of surface roughness
α	Non-dimensional roughness parameter
β	Radius of curvature of asperity peaks
δ_N^{RMS}	Normalised displacement in RMS model
μ	Coefficient of friction at start of sliding
μ′	Surface asperity parameter
η	Density of asperities distribution per unit area
υ	Poisson's ratio
σ	Combined RMS roughness of the two surfaces
σ_y	Yield stress at contact

✉ F. N. Altuhafi
f.altuhafi@ucl.ac.uk

[1] University College London, London, UK

1 Introduction

Hertz contact theory [9] is widely used to model the discrete behaviour of granular materials including soils, ballast or rock fill. The Hertz solution describes the deformation during normal loading of two contacting smooth elastic spheres pressed against each other. For most granular materials, however, the presence of surface asperities can affect the behaviour at the contact, for example the contact stiffness is reduced, resulting in a softer response of the grain assembly (e.g. [14]. Modifications to the Hertz model to include roughness effects have been numerous and varied. Greenwood and Tripp [7], then Greenwood et al. [8] and Johnson [11] considered that the behaviour at the contact of rough spheres is fully elastic, with both the asperities and bulk surface at the contact deforming according to Hertz theory. In most models, the roughness, which affects the normal load–deflection response, is represented by the root mean square (RMS) value of asperity heights, although more recently the concept that most surfaces are fractal in nature has been used. Yang et al. [31] showed how the surface fractal dimension gives a measure of the irregularity of soil grains, complementing the RMS roughness for a

better representation of the surface morphology. The model proposed by Pohrt and Popov [18], which uses the fractal dimension as a key parameter, was successfully implemented by Tolomeo and McDowell [23] into DEM for more realistic predictions of railway ballast behaviour. Other models, such as those proposed by Yip and Venart [29] or Bahrami et al. [4], consider that the contacting bodies comprise a plastic crust (the asperities) overlying an elastic bulk. Altuhafi et al. [2] compared predicted data using Yip and Venart [29] and Pohrt and Popov [18] models and although those models were developed for engineered surfaces, good agreement was found with experimental data obtained from particle-to-particle tests on machined granite surfaces.

In most elastic models there is a power relation between normal stiffness, K, and normal force, F, with the exponent equal to 1/3 for Hertz [9] ($K \alpha F^{1/3}$; 1/2 for Goddard [6] for low loads, or linked to the fractal dimension for Pohrt and Popov [18], with values between 0.51 for smooth surfaces (fractal dimension equal to 2) and 0.77 for very rough surfaces (fractal dimension equal to 3). In the two latter models, as well as in Yip and Venart [29] model, the stiffness reverts to being Hertzian at higher loads. Goddard's [6] assumption was that the change in stiffness is gradual and results from the contact geometry moving from being initially sharp to becoming more rounded with larger loads. Pohrt and Popov [18] on the other hand have linked the load exponent and the transition to Hertzian behaviour to the surface roughness and fractal dimension. In this paper, experimental data will be compared to predicted responses by Hertz (H), Greenwood et al. (RMS) and Pohrt and Popov (P&P) models. Details on the use of the Pohrt and Popov model [18] for soil behaviour have been given in Altuhafi et al. [2] and Tolomeo and McDowell [23].

From recent experimental evidence, it has been shown experimentally that plastic deformation can occur at the contact, and extend to the bulk shape at the contact point (e.g. [27]. This transition from elastic behaviour to plastic behaviour at contacts has been also noted in non-geomaterials such as industrial granules [1]. While elastic models will fail to predict the response after the onset of plastic deformations [2], most of the available elasto-plastic contact models tend to assume that the transition to plastic deformation occurs at the asperities in contact, however there are no or limited studies on the deformation of the bulk. Thornton [22] suggested modelling the plastic behaviour at contacts subjected to normal loading by assuming that the particles yield at a contact stress corresponding to a cut-off in the Hertzian pressure distribution, after which the displacement is plastic and the relationship between normal load and displacement is linear i.e. the contact will deform with constant stiffness. This is in agreement with experimental data obtained on granite contacts presented by Altuhafi et al. [2], who also suggested that Hertz model can be used to simulate the contact behaviour during normal unloading, as was also suggested by Thornton [22] and implemented by Tolomeo and McDowell [23]. Zhao et al. [30] modelled the transition from elastic to fully plastic deformation at the contact of two nominally flat rough surfaces as occurring only in the asperities, with plastic deformations initiating when the maximum Hertz contact pressure reaches 60% of the material hardness ($0.6H_V$). The model was developed based on the deformation of single asperities, but it can be extended to the whole contact area. At high normal loads, when asperities are fully deformed and the stresses exceed the material strength, the bulk would be expected to deform plastically too.

Plastic deformation may affect the lateral loading even more, as existing models based on elastic deformations have so far been found unsuitable to simulate the contact behaviour of sand grains (e.g. [13] or railway ballast (e.g. [26], often predicting a response one order of magnitude stiffer than the test data.

Exhaustive comparisons between real test data and contact models are limited in the literature, due to both the lack of good quality data or sometimes any experimental data at all, and to the difficulty of applying those models to real materials. An accurate representation of the contact morphology, and measurement of the curvature at the contact, are necessary to use most models, but in natural materials the shape, particularly at the contact, can be complex and at a scale that makes measurements non-straightforward. Yao et al. [27] compared test data from sand particles loaded normally against a rigid platen with predictions by Hertz model and by Greenwood et al.'s [8] model showing that generally the latter model showed a close representation of the data unless severe plastic deformation had occurred at the contact, then the load–deflection behaviour diverted significantly from the simulated response, being much softer. In Yao et al.'s experiments, plastic deformations for different load levels were measured using the profile obtained by interferometry, and a relationship was established between the amount of deformation and the radius of curvature. Altuhafi et al. [2] who tested granite particles machined to defined geometry, compared their response with existing elastic models: Hertz (H), Hertz with roughness (H-RMS), Pohrt and Popov (P&P) and models with plastic asperities (Yip and Venart, Bahrami et al.), and also found from the experimental results that small radii of contact curvature led to larger plastic deformations and greater divergence from the model predictions. For particles that deformed predominantly elastically, the models by P&P and Yip & Venart showed the best agreement with the test data.

In this paper, the link between the onset of plastic deformations and the change in stiffness at the contact is examined based on test data in both normal and lateral loading. The tests were carried out on two types of natural railway ballast and some granite particles machined to have shapes

with defined curvatures, such as spheres and cones, for easier implementation of the models.

2 Materials

Two railway ballasts commonly used in their respective countries were chosen for testing, a granodiorite ballast retrieved from Mount Sorrel, U.K., and a latite basalt ballast from the New South Wales region, Australia. In order to achieve a point-flat contact, a naturally pointed ballast stone was selected to form a single point contact on a naturally formed flat surfaced ballast stone of the same material. The mineralogy of the Mount Sorrel granodiorite mostly consists of feldspar, plagioclase, potassium-feldspar and quartz [20]. Its main mechanical properties are listed in Table 1. The Poisson's ratio used in the calculations was 0.25, a typical mean value for granite [5]. The physical and durability attributes of the latite basalt were given by Indraratna et al. [10]. Its modulus of elasticity E and Poisson's ratio were taken as 57GPa and 0.25 respectively [19], for the purpose of model calculations.

As well as being tested in their natural shape, some grains of granodiorite ballast were machined to achieve a defined geometry, such as spheres of different diameters, flat surfaces and conical shapes. The roughness of the spherical stones was controlled by using a stone polishing tumbler while the flaws in the flat surfaces were smoothed using polishing paper. A V8 Stereo-Discovery Microscope was used for surface image acquisition while analysis of the images was carried out using the ConfoMap7 software (equivalent to Mountains 7.4). For non-flat surfaces, natural or machined, the radius of curvature at the contact was determined from microscope images as the mean value on two orthogonal directions using the best fit circle in the local profile where the contact is taking place. An example of radius determination is shown in Fig. 1.

Table 1 Mechanical properties of Mount Sorrel granite used in this study

Specific gravity G_S	2.68
Unconfined Compressive strength (MPa)	176.4
Poisson's ratio, ν	0.25
Young's Modulus (GPa)	60.6
Shore Hardness*	77 this is equivalent to 639 kg/mm^2 in Vicker's hardness**

*Shore Hardness is a measure of the resistance a material has to indentation. A diamond-tipped hammer is manually dropped vertically and freely from a height on to a horizontal, polished test surface

**The Vickers hardness, also referred to as a micro-hardness test, is carried out by observing the area of the indentation caused by a diamond pyramid indenter under vertical load

2.1 Inter-particle apparatus

The particle-to-particle tests were carried out using the inter-particle apparatus designed at UCL and described in Wong and Coop [25]. The apparatus was developed to investigate the contact behaviour of coarse-grained materials, with vertical and horizontal load capacities of 1 and 0.5kN respectively. Two particles (stones) can be mounted on platens and subjected to loads along three axes that are concentric with their contact (Fig. 2). In each axis, the load is applied by a linear actuator and measured with a load cell with a resolution of about 0.01–0.02N. A non-contact displacement transducer along each axis is used to monitor the displacements with a resolution of 10^{-2} µm. The lower platen is held on a sled, under which is a three-point bearing system, for which the friction was calibrated, even if it was barely significant. A purpose-written software that allows control of each axis in either a force or displacement mode is used to control the load application and to log the data during the test. To reduce compliance at the contact with the platen, the stones were cut flat on the side where they were attached to the platen by an epoxy resin glue, using a small thickness of glue to ensure minimum compliance.

Details of the tests carried out are listed in Tables 2, 3 and 4. In all the tests, initial contact between the particles was made using a slow displacement control mode (0.1 mm/h) until the normal load reached 10N, then force control was

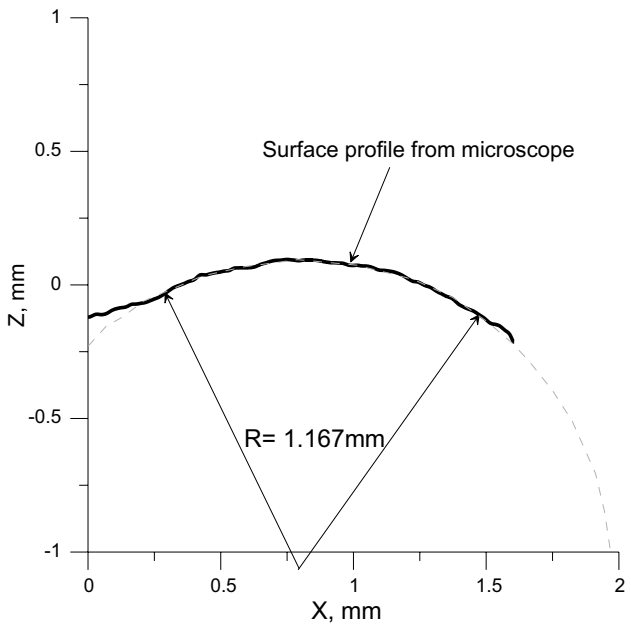

Fig. 1 Radius of curvature estimation at contact point from local microscope profile for Test BB12 in X–Z direction

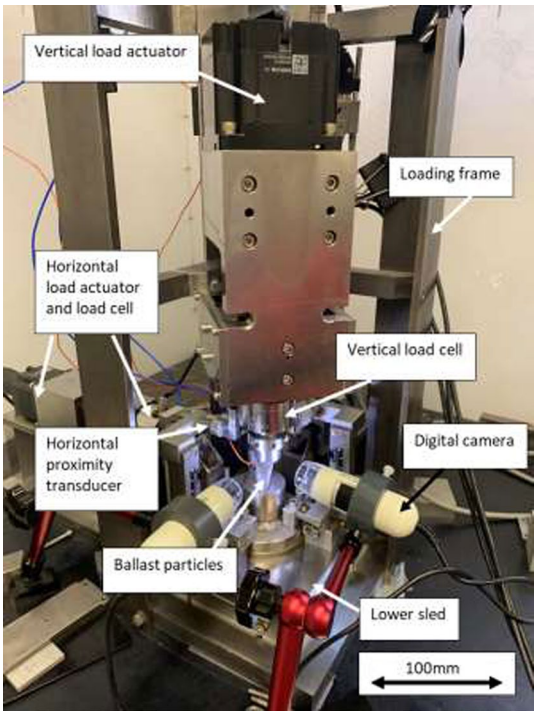

Fig. 2 Inter-particle apparatus

started. This was done to avoid heavy impact between the two surfaces at the instant of contact, which would have occurred had a force-controlled loading been used at the start.

The roughness values reported in this paper are the root mean squares of surface heights (RMS or Sq) of an area of 0.2×0.2 mm at the area where the contact is expected to take place. Height measurements on the sample were made from Z-stack images obtained by the microscope using a magnification of 84X, for which the total area of view was $1.62\ \text{mm} \times 1.34$ mm. Full analysis of the surface can be made using the microscope software to provide statistical data of the surface topography which also has the ability to remove the surface shape effect using different degrees of polynomial fittings to the surface. The fractal dimension of the surface D_f was also calculated, using the box counting method. The values of surface roughness reported here were obtained after removing the effect of shape using a polynomial function in the ConfoMap7 software.

2.2 Plastic behaviour during normal loading

Altuhafi et al. [2] showed that during normal loading of spherical granite ballast with diameter between 12 and 18 mm, no or insignificant plastic deformation takes place at the contact, and any small plastic deformation is limited to

Table 2 Test details for conically shaped tests

Test ID	Description	Properties	
FC5*	Cone against flat	Cone base diameter mm	5.15
RFC10*	Cut ballast surface in multiple cyclic loading stages with sample surface morphology monitoring between stages. Five stages were conducted:	Cone height mm	9.90
		Cone tip curvature radius mm	0.32
	1st: load to 20N then unload	Cone surface roughness S_q µm	3.67
	2nd: load/unload to 20N then 40N	Cone fractal dimension D_f	2.05
	3rd: load/unload to 20, 40 and 80N	Flat surface: S_q µm	1.95
	4th: load/unload to 20, 40, 80 and 150N	Flat surface: D_f	2.02
	5th: load/unload to 20,40, 80, 150 and up to failure load		
	Cone against flat cut ballast surface in multiple cycles of load/unload to 20, 40, 80, 150 and 300N without removing sample between cycles	Cone base diameter mm	10.75
		Cone height mm	10.97
		Cone tip curvature radius mm	0.96
		Cone surface roughness S_q µm	5.04
		Fractal dimension D_f	2.66
		Flat surface: S_q µm	2.47
		Flat surface: D_f	2.17
FC15	Cone against flat cut ballast surface in monotonic compression to 300N maximum normal force	Cone base diameter mm	15.23
		Cone height mm	11.49
		Cone tip curvature radius mm	0.64
		Cone surface roughness S_q µm	2.48
		Fractal dimension D_f	2.06
		Flat surface: S_q µm	1.97
		Flat surface: D_f	2.36

*Some data of these tests is presented in [2]

Table 3 Details of tests on natural Latite basalt ballast

Test ID	Mean radius of top stone at contact, mm	Combined roughness of two surfaces, μm	D_f		Max Normal load, N
			flat	point	
BB2	2.94	12.9	2.07	2.15	150
BB12	0.50	10.7	2.08	2.17	200
BB1_AH	4.23	6.88	–	–	100
BB2_AH	2.80	–	–	–	100

Table 4 Details of tests subjected to lateral loading

Test ID	Description	R_1 mm*	R_2 mm*	S_{q1} μm**	S_{q2} μm**	$D_{f1}{}^+$	$D_{f2}{}^+$
SS(18–18)[1]	Relatively smooth granite spheres. Tested in normal loading to 100N. Lateral loading (post sliding) at both 20N and 100N normal load	8.76	8.63	1.56	1.84	2.21	2.23
VS(18–18)	Very smooth granite spheres tested in normal loading to 200N. Pre-slip lateral loading at 20N, 50N, 100N, 150N and 200N	8.27	7.90	1.07	1.50	2.01	2.20
GB2	Natural granite ballast tested in normal loading up to 150N. Pre-slip lateral loading at 20N, 50N, 100N and 150N	3.92	∞	14.10	10.10	2.13	2.09

1 some data of this test is presented in [2]

*R_1 and R_2 are the radius of curvature of the top and lower surfaces in contact respectively

**S_{q1} and S_{q2} are the root mean square of the roughness of the surfaces in contact

$^+D_{f1}$ and D_{f2} are the fractal dimension values for the top and lower surface in contact respectively

changes in the surface and does not extend to the bulk. The contact behaviour can therefore be represented to an acceptable accuracy by an elastic contact model that includes roughness such as the RMS model [8], or by models for rough fractal surfaces such as the P&P model [18]. However, when there is high curvature at the contact, the stresses concentrated on the small contact area are greater, which can result in damage extending to the core shape of the particles. Figure 3 shows images of the deformation taking place at the contact between a conically shaped granite particle and a flat granite surface (Test FC5). The mean radius of curvature at the cone tip was 0.32 mm. The images show the development of deformation with the increase of normal load from 0 to 150N. Changes in the cone tip profile are shown in Fig. 3g and changes in the flat surface at the area of contact in Fig. 3f, for loads of 80N and 150N. It can be seen that most of the plastic deformation of the bulk shape is taking place in the flat surface, increasing with load level, while no significant change in cone tip shape is noticed at these load levels.

Figure 4 shows the displacement—force relationship for three cone-flat contact tests for which the dimensions and properties of the cones are given in Table 2, in which the test ID names indicate the approximate cone base diameter (5, 10 and 15 mm). It is clear from Fig. 4 that the response to normal loading is mainly governed by the cone tip curvature, and not other shape properties, least of all the cone base diameter or height. In test FC5, with the smallest cone tip radius of 0.32 mm, a higher normal displacement was measured compared to test FC15 (cone tip radius 0.64 mm) and RFC10 (cone tip radius 0.96 mm). The larger contact area associated with larger contact radii results in a lower concentration of stresses at the contact area, which explains the smaller deformation. Examination of the topology showed that clear shape changes occurred at higher loads, after reaching 20N. On the other hand, the limited deformation at low normal load levels meant that application of elastic models to the behaviour at lower range of load might be possible. Figure 5a and b show predictions by the two rough elastic models, P&P and RMS, as well as Hertz for tests FC5 and RFC10 for a normal load range up to 20N. For both tests, the Hertz model predicts stiffer behaviour than the experimental data. Test RFC10 shows a good agreement with both rough elastic models RMS and P&P in this load range, while FC5 which has the smallest radius of curvature diverts from these models much earlier, at about 7N normal load, and starts to deform with the stiffness remaining constant after reaching this load, indicating that plastic deformations started at even lower normal loads.

It is not possible to measure the stresses at the contact of rough surfaces accurately unless the real contact area is measured. The real contact area can be very different

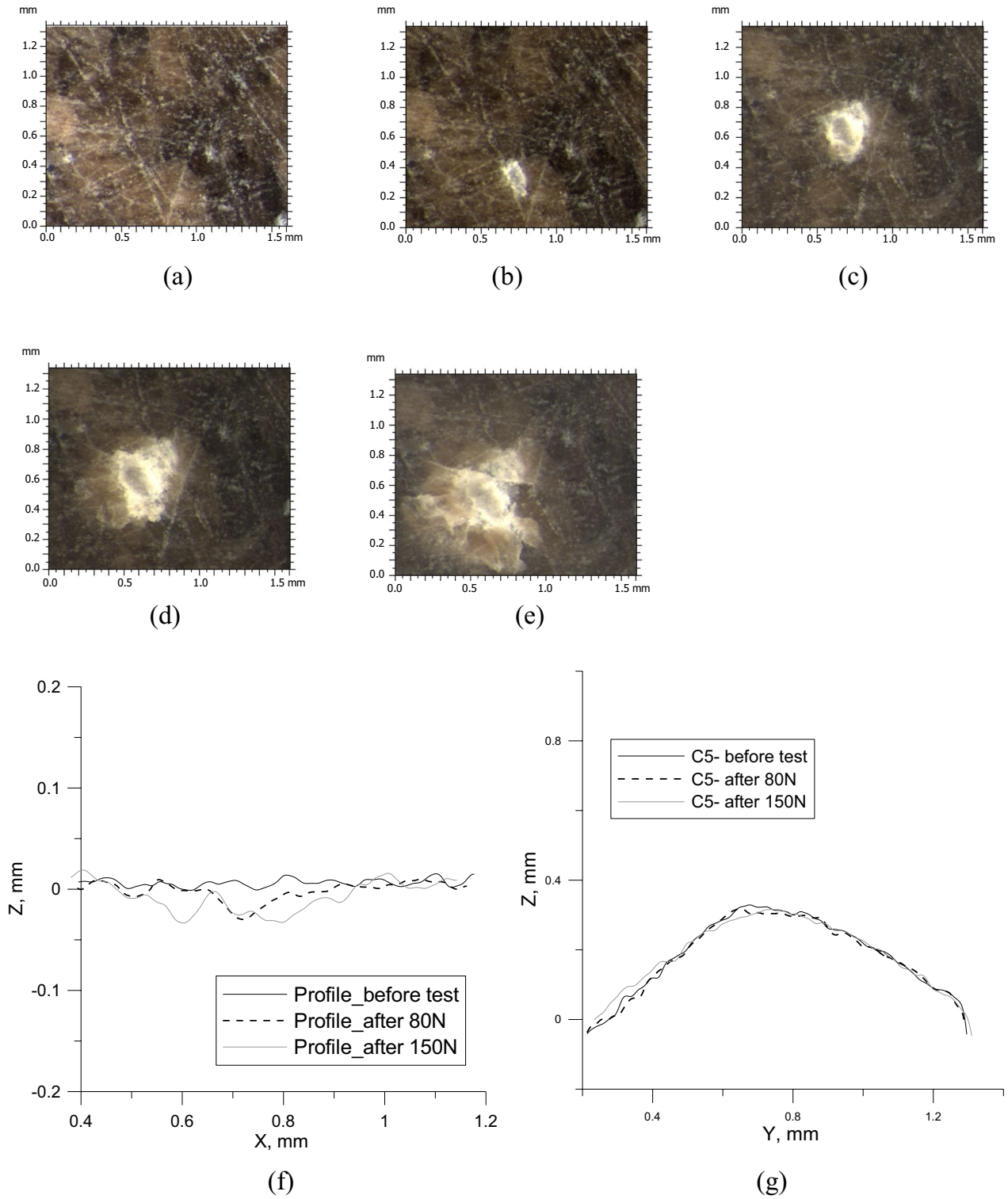

Fig. 3 Images showing flat surface damage in cone-flat contact test FC5 after different normal loading stages, **a** before test, **b** after 20N, **c** after 40N, **d** after 80N, **e** after 150N, **f** profile change of the flat surface at area of damage, **g** profile change of the cone tip

from the nominal area estimated in most elastic models. It can be estimated from the area of the islands formed by the smaller contacts within the nominal area [17], but for smooth spheres, an approximation of these stresses can be obtained from the radius of the nominal area a_H, proposed by Hertz [9]:

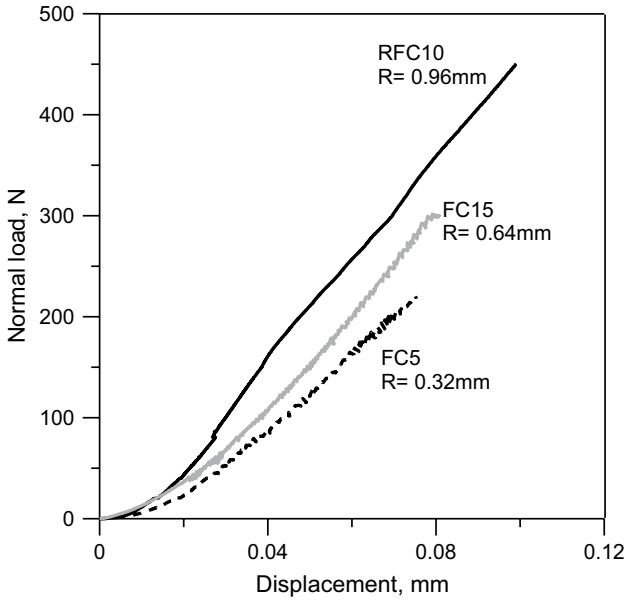

Fig. 4 Three normal compression tests of cone to flat shaped granite contacts with different cone dimensions and surface properties

$$a_H = \left(\frac{3PR}{4E^*}\right)^{1/3} \tag{1}$$

in which P is the load normal to the contact area, R is the equivalent radius of curvature of the two surfaces in contact; $1/R = 1/R_1 + 1/R_2$, and E^* is the combined elastic modulus of the two surfaces in contact and can be calculated from the relation $1/E^* = (1-\nu_1^2)/E_1 + (1-\nu_2^2)/E_2$, where ($R_1$, E_1, ν_1) and (R_2, E_2, ν_2) are the radius of curvature, modulus of elasticity and Poisson's ratio for the first and second sphere respectively. An estimation of the maximum stress p_0 at the centre of the contact can be obtained from the equation:

$$p_0 = \frac{3P}{2\pi a_H^2} = \left(\frac{6PE^{*2}}{\pi^3 R^2}\right)^{1/3} \tag{2}$$

In Fig. 6, the normal stiffness for three cone-flat compression tests is plotted against the predicted maximum Hertzian pressure using Eq. 2. The corresponding stiffness-pressure relationships as predicted by the Hertz model are also plotted for each of these tests. The simulated stiffness increases continuously with the contact stress level, while the experimental data suggest a limiting value of stiffness, reached when the maximum Hertzian pressure approaches values between 45 and 100% of the Vicker's hardness value, H_v of 639 kg/mm^2 reported for the Mount Sorrel granite (Table 1).

For contacting bodies of similar material, it was shown by Tabor [21] that when contact stresses reach 60% of the material hardness (H_v), yielding will start at the contact or

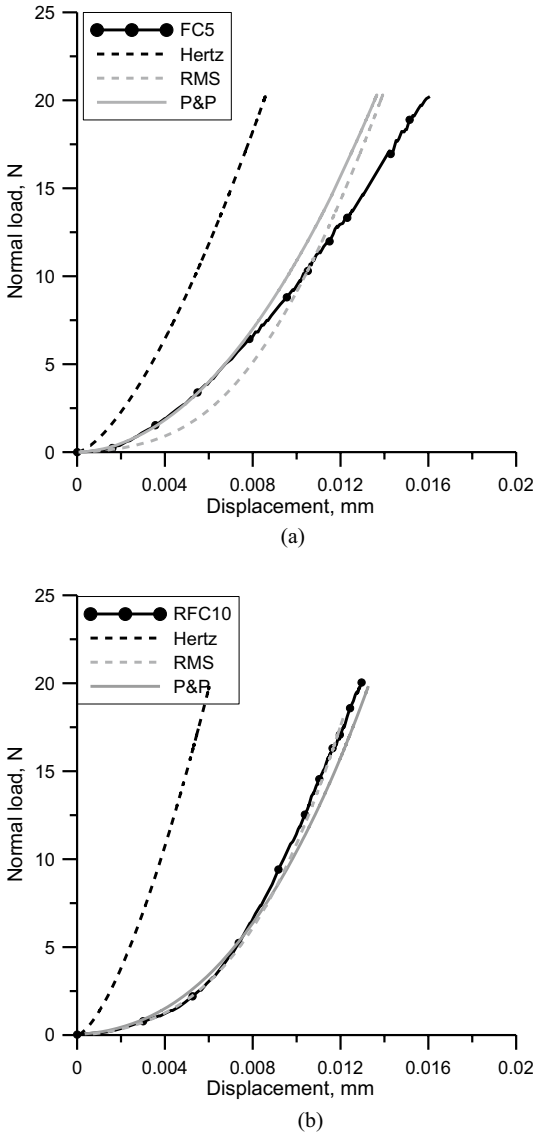

Fig. 5 Modelling of normal compression of contact at low loads up to 20N, **a** FC5, **b** RFC10

asperity and plastic deformation will take place. The value of $0.6H_v$ is shown in Fig. 6 for the granodiorite as a vertical dashed line. Although the experimental data do not yield at exactly $0.6H_v$ contact pressure, probably due to the mixed mineralogy of the granodiorite and therefore the hardness not representing necessarily that of the contact asperities that yielded, it seems reasonable to interpret that the contact surfaces for these tests started to suffer from plastic deformation, with a constant stiffness, at about this value of maximum stress.

In Thornton's [22] model, contacting particles follow Hertz load–displacement law until a contact yield pressure (σ_y) is reached and plastic deformations start, after which the load–displacement follows a linear relationship of slope

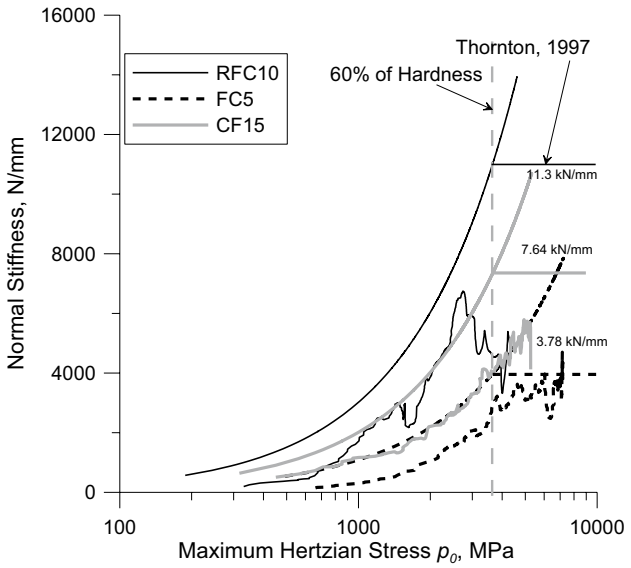

Fig. 6 Maximum stress at contact as predicted by Hertz plotted against normal stiffness for three conically shaped granite particles compressed against flat granite surfaces. Thornton [22] model for elastic-perfectly plastic model is also shown

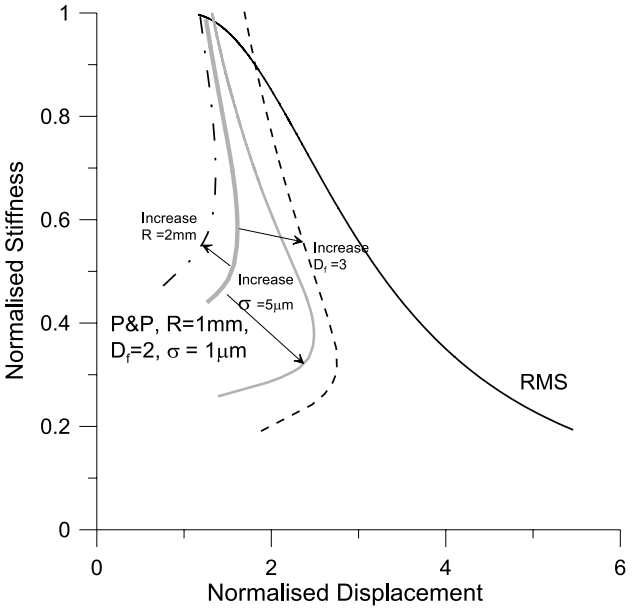

Fig. 7 Normalisation of two elastic models (RMS and P&P) to the Hertz model

$\pi\sigma_y$ R, i.e. with a constant stiffness. The response predicted by Thornton's model for tests RFC10, FC15 and CF5 is shown in Fig. 6, using the contact yield stress as 0.6 Hv to be consistent with Tabor [21] and our experimental data. The constant stiffness takes different values depending on the value of stiffness reached until yield, which depends on the combined radius of the particles in contact.

2.3 Normalisation of contact behaviour during normal loading

To identify more clearly the start of plastic deformation during normal loading, and whether this behaviour is an intrinsic property of the material, a normalization of the data is proposed: both the normal displacement and normal stiffness are divided by the corresponding displacement and stiffness predicted by Hertz model at the same load level, using the following formulae:

$$\delta_N^H = \frac{a_H^2}{R} = \left(\frac{9P^2}{16RE^{*2}}\right)^{1/3} \tag{3}$$

$$K_N^H = \left(6PRE^{*2}\right)^{1/3} \tag{4}$$

With such normalisation, the normal displacement, δ_N divided by Hertz displacement value, δ_N^H at the start of the test (low loads) will be high for an ideal rough contact, decreasing with increasing load level as the normal stiffness approaches the Hertz stiffness and the ratio of normal stiffness, K_N divided by Hertz stiffness, K_N^H eventually reaches unity when all asperities have yielded. It must be noted that since the displacement is cumulative, the ratio of normal displacement/Hertz displacement will never reach unity but will be asymptotic to it at large displacements.

The experimental data are compared with predicted stiffness for two models, the RMS [8, 28] and P&P models [18]. Figure 7 shows the trends predicted by these two models within the normalised plot. A brief description of the models and their assumptions is given below.

(a) RMS model

Yimsiri and Soga [28] proposed an empirical formula based on data from Greenwood et al. [8] who assumed that the apparent nominal contact area between rough surfaces, a^*, is larger than that for smooth surfaces, and can be related to the Hertz radius of contact area, a_H, by a function of the parameter α, where:

$$\alpha = \frac{\sigma R}{a_H^2} \tag{5}$$

where σ is the combined roughness value of the two surfaces in contact, and is obtained by the equation $\sqrt{{S_{q1}}^2 + {S_{q2}}^2}$, where S_{q1} and S_{q2} are the RMS values of the two surfaces in contact.

The parameter α gives an indication of the relative magnitudes of the asperities and the mutual displacement of

the particles. The proposed equation by Yimsiri and Soga [28] is:

$$\frac{a^*}{a_H} = \frac{-2.8}{\alpha + 2} + 2.4 \tag{6}$$

From which the RMS normal displacement, δ_N^{RMS} can be calculated:

$$\delta_N^{RMS} = \frac{a^{*2}}{R} \tag{7}$$

The RMS normal stiffness can be found from the derivative of normal force P with regards to normal displacement δ_N^{RMS} and by substituting Eqs. (1), (5) and (6) into Eq. (7). The RMS normal stiffness K_N^{RMS} can be calculated:

$$K_N^{RMS} = \frac{dP}{d\delta} = \frac{PR}{2a^*}\left(\frac{a^*}{3} - \frac{5.6a_H.\alpha}{3(2+\alpha)^2}\right)^{-1} \tag{8}$$

In this model α alone controls the relation of the normalised stiffness, ${}^*K_N^{RMS}$ and normalised displacement ${}^*\delta_N^{RMS}$, as can be seen from the following equations:

$${}^*K_N^{RMS} = \frac{1}{\sqrt{\delta_N}\left(\sqrt{\delta_N} - \frac{5.6\alpha}{(2+\alpha)^2}\right)} \tag{9}$$

$${}^*\delta_N^{RMS} = \left[\frac{-2.8}{\alpha + 2} + 2.4\right]^2 \tag{10}$$

The equations above predict a unique single curve, shown in Fig. 7, with values of $({}^*\delta_N^{RMS}, {}^*K_N^{RMS}) = (5.76, 0.174)$ at small displacements, reaching (1, 1) at large displacements. In reality, because the stiffness at the contact of rough surfaces is lower than that predicted by Hertz, the deformation at rough contacts will necessarily exceed the Hertz displacement, thus the ratio of displacement over Hertz displacement will be larger than one when the RMS model reverts to Hertz. This is seen clearly in the obtained data which will be presented in this paper, in Fig. 8. On Fig. 7 are also shown predicted curves when using Pohrt and Popov model. Details of how the curves were obtained are given below.

(b) Pohrt and Popov model (P&P) for fractal rough surfaces

In the proposed normalisation plot shown in Fig. 7, unlike the RMS model, a unique curve cannot be predicted by the model proposed by Pohrt and Popov [18], as the predicted response depends on parameters that, unlike α above, are not normalised. In the P&P model, the stiffness is expressed as:

$$K_N^{P\&P} = \frac{\pi\sqrt{A_0}E^*D_f}{10} \cdot \left(\frac{P}{\sigma E^*\sqrt{A_0}}\right)^{0.257D_f} \tag{11}$$

where D_f is the fractal dimension of the surface, and A_0 is the area of contact when all asperities have yielded and full contact has taken place, i.e. the behaviour becomes Hertzian. The full contact area A_0 can be calculated by:

$$A_0 = \frac{3}{4}\pi^{3/2}R\sigma\left(\frac{20}{\pi^{3/2}D_f}\right)^{1/0.257D_f} \tag{12}$$

The displacement is calculated simply from the change in normal stiffness and normal force. The parameters representing the surface, the combined curvature (1/R), the combined roughness σ and mean fractal dimension can all affect the shape and position of the predicted curve as shown in Fig. 7. While an increase in R will move the curve further to the left side of the chart, increasing either the fractal dimension D_f or the combined roughness will move the curve to the lower right of the chart with no tendency to reach the Hertz model prediction (1, 1).

Figure 8a presents normalised data obtained from the three cone-flat contact tests presented earlier. The curves predicted using the RMS and P&P models are plotted for parameters determined for test RFC10. As seen above, the curve for the RMS model is unique, therefore the experimental data from all three tests can be compared with it but it is seen from the figure that only data from RFC10 agrees well with the normalised RMS model curve. This will be discussed later in this section. It seems that the normalised stiffness of the experimental data is not increasing beyond a certain value for all these tests. This clearly shows that the maximum stiffness of the material has been reached and the material is deforming with constant stiffness after this point indicating yielding of the material at the contact point, this agrees with what Thornton [22] presented in his model for normal contact of elastic-perfectly plastic spheres. Note that for test FC15, only data around the yield are plotted as the data at the start of the test were inadequately logged. For tests FC5 and RFC10, following yield the normalised stiffness clearly reduces: this is caused by the actual stiffness remaining constant while the Hertz stiffness increases with the applied force. In Fig. 8b, the normalised cone-flat test curves are plotted together with those for test RS(18–18) that were performed using two contacting rough granite spheres (data from [2], as well as two contact tests on natural granite ballast behaviour SC11 and SC14 (data from [26]). It is clear that the increase in stiffness in all of these tests ceases when the contact stiffness reaches about 70% of Hertz stiffness, indicating that extensive plastic deformation starts for this material before the cross-over to the Hertz model, regardless of the shape or the texture of the surface in contact, and this

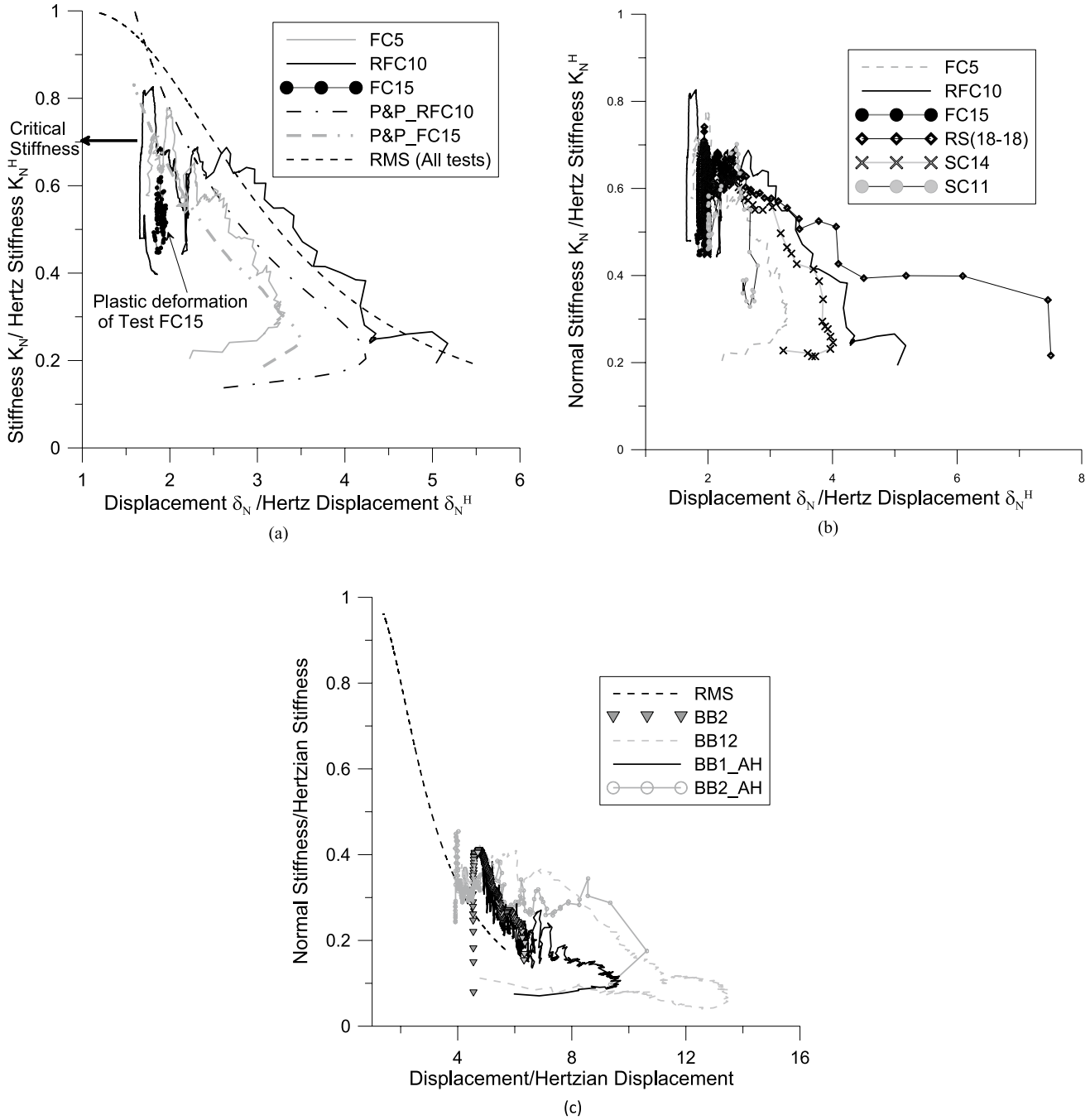

Fig. 8 Normalisation of data of normal loading of particles with different shape and morphologies, **a** granite cone to flat data compared to models, **b** data for rough granite spheres RS(18–18) and data of natural granite ballast stones SC11 and SC14, **c** normalisation of natural basalt ballast data

ratio is an intrinsic property of the material which we will call critical normal contact stiffness.

The same normalising method was applied to results from four normal loading tests obtained on natural basalt ballast from Australia. "Natural" here refers to the ballast being in its as supplied condition, i.e. a crushed rock, with no surface preparation. Details of the tests are given in Table 3 and the responses in Fig. 8c are compared to the normalised behaviour predicted by the RMS model for this material. The contact was made between a relatively flat surface (for which R was considered to be ∞) and a top pointed stone. From the normalised data shown in Fig. 8c, extensive plastic deformation seems to take place early, deforming thereafter at the critical normal contact stiffness of around 35% of the

Hertz stiffness. All tests data plot to the right of the predicted RMS model curve, indicating that for this basalt material the model tends to underestimate deformations. This contrasts with the granite for which RMS model overpredicted the displacement.

The discrepancies between the experimental data and the curve predicted by the RMS model may arise from the fact that Eq. (6) proposed by Yimsiri and Soga [28] neglects some features of surface morphology such as the intensity of peaks in the contact area and the average roundness of peaks which were originally considered in the data presented by Greenwood et al. [8] by the parameter $\mu\prime$, as was noted by Altuhafi et al. [2]. In which $\mu\prime = (8/3)\sigma\eta(2R\beta)^{1/2}$, where η is the density of asperities per unit area and β is the radius of curvature of asperity peaks, assumed to be constant for each surface.

Figure 9 shows the test data taken from Altuhafi et al. [2] on shaped granite contacts along with the original data from Greenwood et al. [8] and the proposed equation of Yimsiri and Soga [28]. The data for the three cone-flat contacts presented in this paper are added to the figure. It appears that only RFC10 follows the proposed equation during the progress of normal loading, starting from high values of α and tending towards zero as the load increases, and the bulk rather than the asperities dominate the deformation. Equation (6) seems to overestimate the a* value in the other two tests (FC5 and FC15), and for these tests the P&P model might give a better representation of the data before yielding takes place, although P&P is an elastic model and the displacements measured are substantially plastic even before yield of the contact bulk shape. Test data obtained by Yao et al. [27] on silica sand, who reported that a transition from the rough elastic model to the Hertz model could be observed well before the start of plastic deformations, are also shown in Fig. 9. While comparing the behaviour of ballast and sand sized particles is difficult because of the much greater roughness of the ballast, by one to two orders of magnitude, the normalisation used in this figure allows better understanding of the accuracy of the RMS model in simulating different material. Note that the hardness of the material on the other hand would affect the comparison less as the hardness of silica sand is only marginally higher than that of granite.

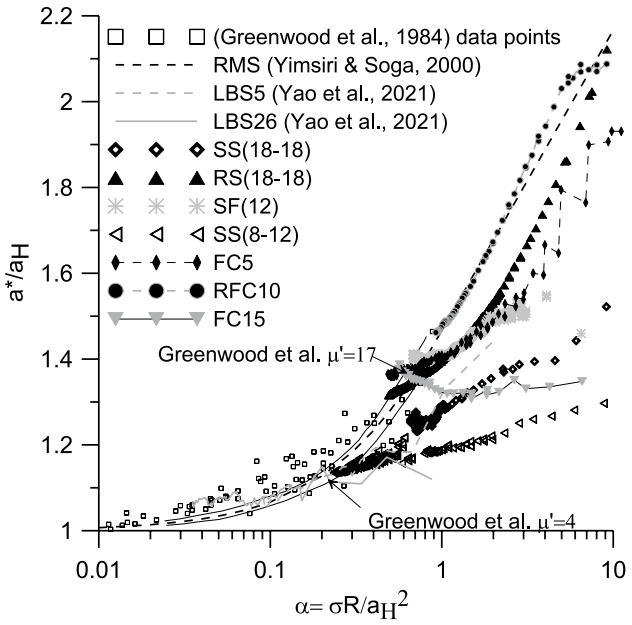

Fig. 9 RMS model equation [28] compared to data for natural and machined geomaterials. The three cone-flat contact tests are added to the figure presented previously by [2]. Data of Greenwood et al. [8] was reproduced by digitizing the original figure

2.4 Behaviour during lateral loading and lateral stiffness modelling

Lateral loading on both machined and natural granite ballast contacts was applied to investigate the applicability of the available lateral loading contact models. There are relatively fewer published theoretical models for lateral contact stiffness than for normal stiffness. Most of the available models adopt the Mindlin constitutive law, in which the initial lateral contact stiffness is simply expressed as the normal contact stiffness times the factor $2(1-\nu)/(2-\nu)$, for isotropic elastic interfaces (e.g. [14, 15, 24, 28]), after which the lateral stiffness starts to degrade with the progress of load until sliding occurs. This degradation function simulates the gradual increase of the slip surface until the two contacting bodies slide against each other. Models for rough surface contacts use a similar expression (Eq. 13) but linking the initial lateral stiffness to the normal stiffness from any normal loading contact model which considers surface roughness:

$$K_T = \underbrace{\frac{2(1-\upsilon)}{2-\upsilon}}_{\text{function relating initial lateral stiffness value to normal stiffness}} K_N \overbrace{\left(1 - \frac{T}{\mu N}\right)^{(1/3)}}^{\text{function of degradation}} \tag{13}$$

The ratio between initial lateral stiffness and normal stiffness is common to most elastic models, however the degradation function can vary: Mindlin and Deresiewicz [12], Vu-Quoc and Zhang [24] and Yimsiri and Soga [28] all adopted the exponent of 1/3 to simulate the rate of degradation of the lateral stiffness towards a value of T/N equal to the friction

coefficient μ, at which point the interface is fully developed with no further slip occurring. On the other hand, Paggi et al. [15] proposed a partial slip condition in the contact during lateral loading, where the degradation exponent is a function of the Hurst exponent, H_{st}, of the fractal geometry of the surface. The lateral contact stiffness becomes:

$$K_T = \frac{2(1-\upsilon)}{2-\upsilon} K_N \left(1 - \frac{T}{\mu N}\right)^{(1/H_{st}+1)} \quad (14)$$

in which the Hurst exponent can be determined from the relation ($H_{st}=3-D_f$).

In Fig. 10, the four models for lateral stiffness were considered to simulate the response to lateral loading between two relatively smooth granite spheres under a normal load of 20N (Test SS(18–18)). Four models for lateral loading were investigated: the elastic models of Mindlin and Deresiewicz [12] and Vu-Quoc and Zhang [24], developed for smooth spheres in contact, in which the normal stiffness is predicted by Hertz ($K_N = K_N^H$), the modified equation proposed by Yimsiri and Soga [28] in their RMS model, and Paggi et al.'s [15] model for surfaces of fractal geometry. In this paper the P&P normal loading model was used in conjunction with the model proposed by Paggi et al. [15].

It can be seen from the figure that all the predicted initial lateral stiffnesses are about one order of magnitude larger than the experimental data. The models by Mindlin and Deresiewicz [12] and Vu-Quoc and Zhang [24] give the highest lateral stiffness as they are based on the Hertz normal stiffness for smooth surfaces which is always higher than the stiffness of the rough contact models, while the model by Paggi et al. [15] for fractal rough surfaces predicts a faster degradation and a lower initial lateral stiffness.

(a) Effect of surface roughness on the lateral stiffness

Figure 11a and b show data obtained from two tests in which two contacting granite spheres were subjected to lateral loading under a normal load of 20N: SS(18–18), for relatively smooth machined spheres, and VS(18–18), for very smooth machined spheres, all of approximately similar radius of curvature ranging between 7.9 and 8.8 mm. Details of these tests are given in Table 4. Figure 11a shows the change in lateral load T/normal load N ratio with lateral displacement while in Fig. 11b the stiffness degradation is plotted against the ratio T/N at the pre-sliding lateral stage. The effect of the surface roughness is visible in both the values of initial stiffness, which is lower for rough contacts, and the value of friction coefficient μ at which the lateral stiffness reaches zero and sliding occurs. The μ-values are reached when the value of T/N stabilises, with a μ-value of 0.18 for test VS(18–18) and 0.28 for Test SS(18–18) (Fig. 11a). These values show clearly that the coefficient of friction μ

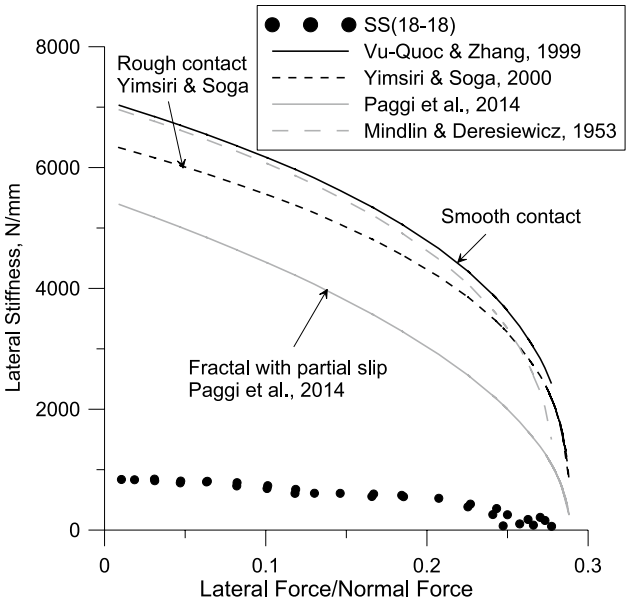

Fig. 10 Lateral stiffness plotted against lateral force/normal force ratio during lateral loading of SS(18–18) at 20N normal load compared to results predicted by four different models of lateral loading

increases with increasing surface roughness when a similar radius of curvature is considered at the contact.

To show the shortcoming of Mindlin and Deresiewicz's model (M&D), in Fig. 11c the normalised mobilised shear stress ratio T/μ.N is plotted against a ratio of the measured displacement by the predicted displacement. On this graph, predictions by the M&D model would plot as a vertical line at an x-axis coordinate of 1. Figure 11c shows a good agreement between the initial response of the very smooth contact VS(18–18) with what would be predicted by M&D, but by start of sliding the particles have experienced around 6 times more displacement than predicted. The divergence of the data from test SS(18–18) from M&D model is even greater and start from the initiation of lateral loading, with sliding happening at a displacement about 14 times that predicted.

(b) Effect of normal load and multiple shearing on the lateral stiffness

Figure 12a presents the degradation of lateral stiffness with T/N in two monotonic lateral loadings under two different normal loads of 20N and 100N (test SS(18–18). Note that because of the uneven surface morphology, a small negative lateral force (i.e. in the backward direction) accumulated during the lateral stress reversal. In most elastic models the normal stiffness, and therefore the lateral stiffness (Eq. 9), are strongly dependent on the normal load, however here no significant difference in lateral stiffness is observed. In Fig. 12a, against the theory for purely frictional materials,

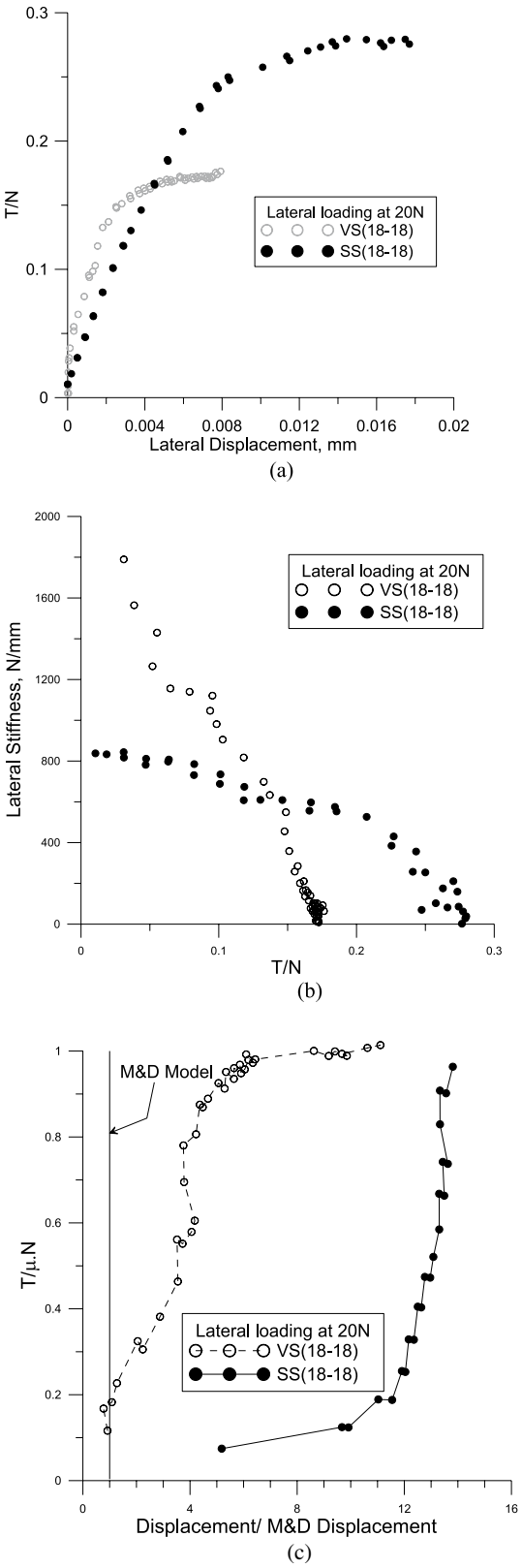

Fig. 11 Behaviour during monotonic lateral loading of relatively smooth spheres of granite SS(18–18) and very smooth spheres VS(18–18) at normal load of 20N. **a** T/N plotted against lateral displacement. **b** Lateral stiffness degradation with T/N (c) Normalised mobilised shear parameter with data/ M&D model displacement ratio

the value of μ at zero stiffness seems to vary for different normal load levels. Previous research on granite ballast had not found any effect of load level on μ for natural samples [25]. This difference is attributed to plastic deformation suffered from the first lateral loading at 20N, leading to a change in surface morphology and therefore a change in the value of T/N at which sliding is initiated. Different test data are compared in Fig. 12b by normalising the T/N values by the corresponding μ value for each test or loading event, and the lateral stiffness by dividing it by Hertz predicted normal stiffness for that set of particles. In this normalised graph the M&D model predicts a unique curve, with an initial value of normalised stiffness equal to $2(1-\nu)/(2-\nu)$ (i.e. around 0.86 for this granodiorite) at the start of shearing. The normalised data of VS(18–18) at the normal load of 20N and the normalised data of the rough contact of RS(18–18) under 100N normal load instead plot much lower, with an initial normalised stiffness value of less than 0.25.

Although the ratio between lateral and normal stiffness typically used in models is derived from the theory of elasticity, one test contacting very smooth spheres (test VS(18–18)) was designed to provide experimental evidence. The spheres were compressed normally to different load levels: 20N, 50N, 100N, 150N and 200N before being subjected to small cycles of lateral loading. These lateral loadings were carefully controlled so as to minimise the displacements pre-sliding and hence minimise damage at the contact. A total lateral displacement of 20 microns was applied at 20N normal load and 50 microns for the higher loads. The degradations of the lateral stiffness with lateral displacement and with the ratio T/N are shown in Fig. 13a and b respectively. A full degradation of the lateral stiffness seems to occur at very small displacements during the first lateral loading at 20N, compared to the subsequent lateral loadings at higher normal loads (Fig. 13a). Sliding under 20N normal load seems to take place just before 7 microns lateral displacement, while for higher loads no sliding is detected within the 50 microns displacement applied during lateral loading, and the stiffness seems to show persistent stable values over the whole lateral loading stage with no clear sign of degradation.

Multiple pre-sliding lateral loadings were also conducted in test GB2 (a natural granite ballast contact) at different normal load levels. Details of the surfaces in contact for this test are given in Table 4. Small lateral displacements of 5 microns and 20 microns were applied at normal loads of 20N and 50N respectively, then 50 microns displacement was applied for higher normal loads. The results, shown in Fig. 14, indicate that unlike what is observed for test VS(18–18), sliding was not initiated for GB2 under 20N (Fig. 14a). Similarly to what was previously noted for test VS(18–18), the initial lateral stiffness does not vary significantly with normal load level. The value of T/N at which

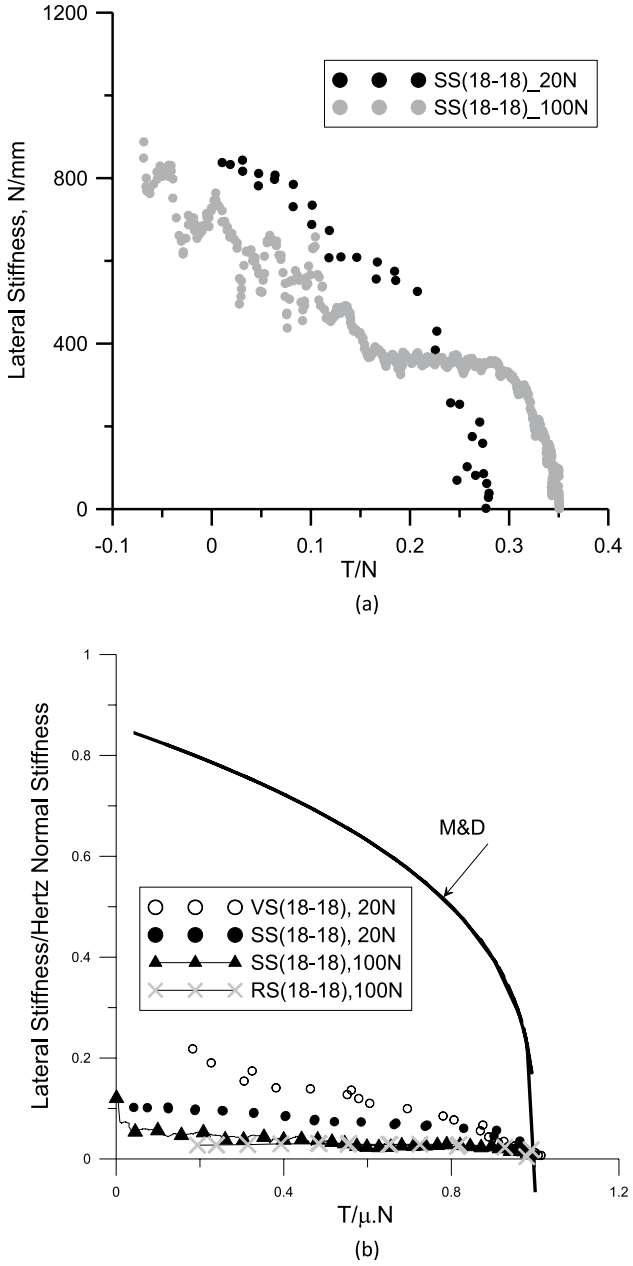

Fig. 12 **a** Lateral stiffness plotted against T/N for two lateral loadings of sphere-sphere contacts for Test SS(18–18) at two different normal load levels. **b** Normalised lateral stiffness by Hertz Normal stiffness versus normalised mobilised shearing parameter for four lateral loading events on three different contacts of sphere-sphere

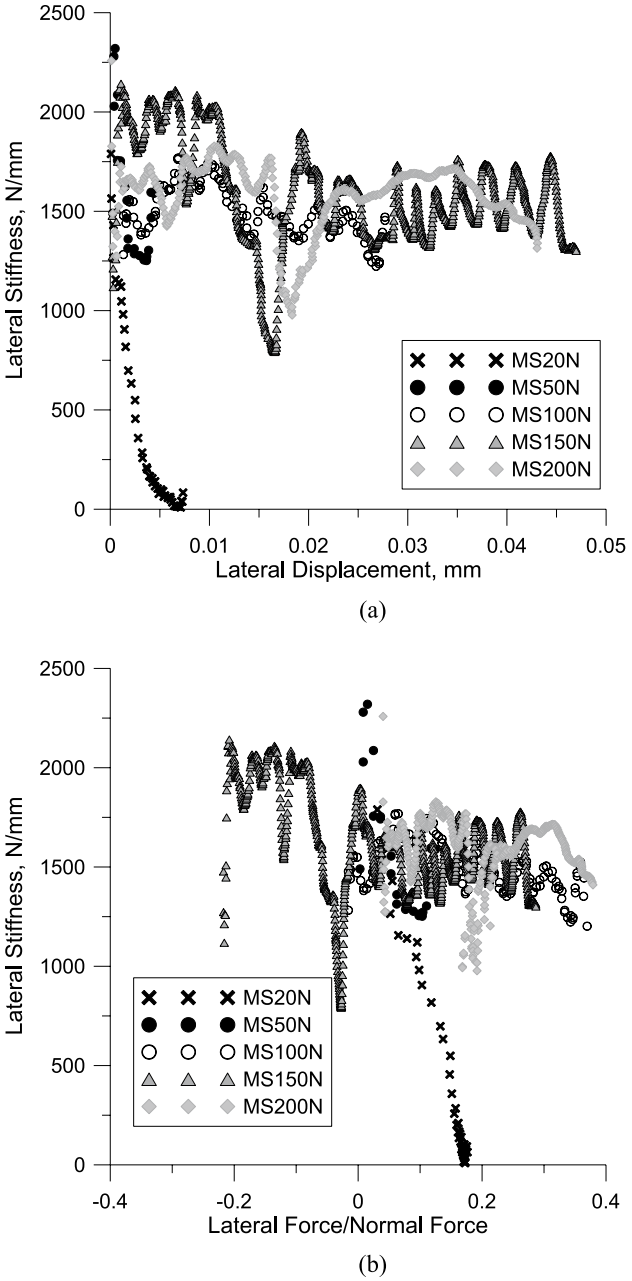

Fig. 13 Lateral stiffness change during monotonic lateral loading at different normal load levels in test VS(18–18): **a** with displacement, **b** with lateral force/ normal force development

sliding would be expected to take place is marked by a decrease in stiffness, and seems to increase at higher normal loads (Fig. 14b). For the stage at 150N normal load, a persistent high stiffness value is observed, which does not seem to degrade over the 50 microns lateral displacement. It is not known to what extent these features simply result from the higher load level but it is interesting to note that a similar behaviour was observed by Altuhafi and Coop [3] in triaxial shearing of the same granite ballast, in which the measured small strain stiffness showed a persistent maximum value in subsequent shearing incidents compared to the first shearing incident. This may indicate that the contact has suffered from plastic deformation during the first loading which caused this change in the stiffness degradation curve.

The initial lateral and normal stiffness determined from the test data (VS(18–18) and GB2; data in Fig. 15) are shown (Fig. 16). The initial lateral stiffness under different

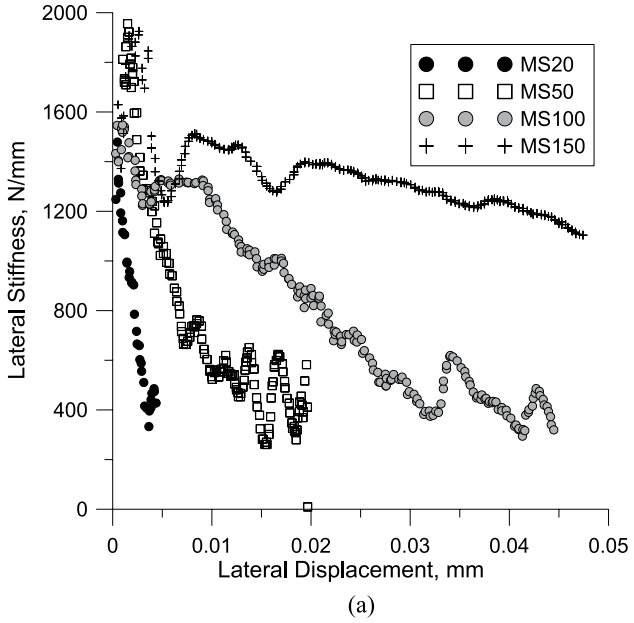

Fig. 14 Lateral stiffness degradation during monotonic lateral loading of GB2 test at different load levels, **a** with displacement, **b** with T/N

normal loads for tests VS(18–18) and GB2 was estimated from Figs. 13 and 14 respectively. For each load level the corresponding normal stiffness was obtained from Fig. 15. The experimental data seem to show that there is a linear relationship between initial lateral and normal stiffness but at a gradient much lower than that predicted by Mindlin ratio (i.e. $2(1-\nu)/(2-\nu)$). While the gradient calculated for the elastic model is around 0.86, the gradient derived from the test data is around 0.05.

(c) Degradation function of lateral stiffness

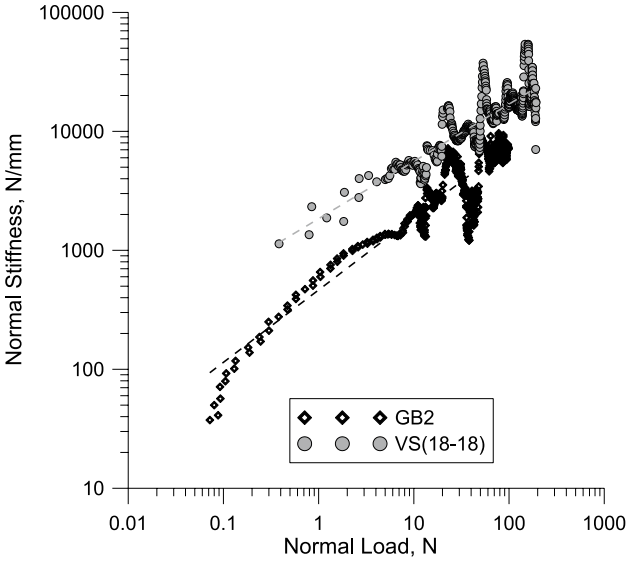

Fig. 15 Normal stiffness plotted against normal load for tests GB2 and VS(18–18)

Figure 17 shows the degradation of lateral stiffness against lateral force for tests VS(18–18) and GB2 during lateral loading under 20N normal load. The degradation data are plotted together with the curves predicted by the contact models [12, 24, 28] which use an exponent of 1/3, and by Paggi et al. [15] which uses a Hurst-based exponent ($1/(1+H_{st})$). It is obvious that none of the models can capture the degradation measured in the tests, and for the data available a simple linear relation would fit them better. It is interesting to note that Parel et al. [16] also found a linear

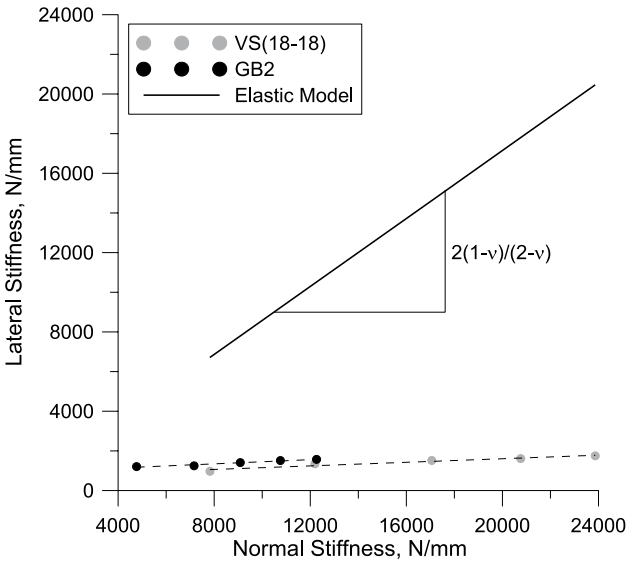

Fig. 16 Lateral stiffness plotted against normal stiffness as predicted by models compared to real data

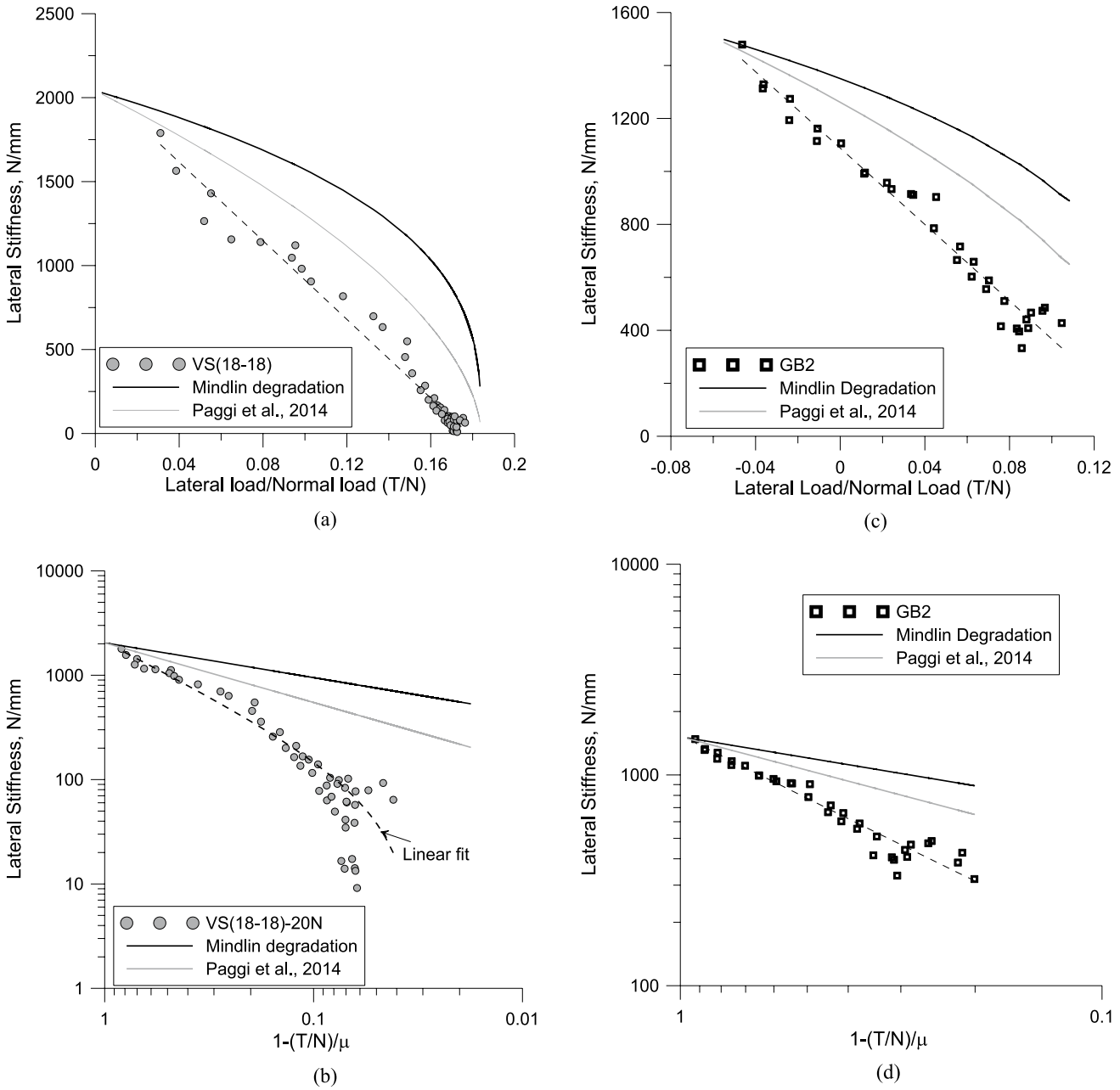

Fig. 17 Degradation of lateral stiffness data compared to degradation of stiffness as predicted by models, **a** lateral stiffness plotted against (T/N) for Test VS(18–18), **b** lateral stiffness plotted against function 1-(T/N)/μ for Test VS(18–18), **c** lateral stiffness plotted against (T/N) for Test GB2 (**b**) lateral stiffness plotted against function 1-(T/N)/μ for Test GB2

relationship between lateral stiffness and lateral load in tests on an alloy Ti–6Al–4V interface.

3 Conclusions

Normal and lateral loading of machined and natural granite particles with different radii of curvature and different morphologies were tested in both normal and lateral loading in an inter-particle testing apparatus. Some tests were also carried out on a natural basalt ballast. The particles were tested pre-failure, where failure means a catastrophic destruction of the contact. The tests yielded interesting results which emphasize the effect of plastic deformation on the behaviour of contacts and the

applicability of elastic models. The following are the main points which can be concluded from this study:

1. In normal loading, contacting particles of small radii of curvature have a small area of contact and therefore higher pressures are expected in the contact area which lead to early plastic deformation (at relatively lower normal load). Elastic models can only be applied before extensive plastic deformation takes place. When plastic deformations extend to the bulk shape of the contact, displacements occur at constant stiffness until failure.
2. The onset of extensive plastic deformation extending to the core shape of the contact takes place when the maximum stress at the contact, which can be roughly estimated using Hertz model, reaches approximately 60% of the material hardness. This is in agreement with Tabor's [21] findings.
3. It is usually assumed that asperity deformation stops at the crossover point from an elastic rough model to the smooth surface Hertz behaviour, which has been observed on relatively smooth surfaces of higher material hardness. However, the data shown here suggest that extensive plastic deformation of rough surfaces starts before, and that the load–displacement behaviour is linear afterwards. For the granite and latite basalt tested here, constant stiffnesses equal to 70% and 35% of the predicted Hertz stiffness were found respectively.
4. Data obtained from lateral loading tests on machined and natural granite particles show that the initial lateral stiffness predicted by most contact models (for smooth and rough surfaces) is around an order of magnitude higher than the measured initial lateral stiffness. The ratio between initial lateral and normal stiffness usually adopted in the models also seems to be well overpredicted.
5. A linear degradation of lateral stiffness with lateral load is noted during the lateral loading of both smooth and rough surfaces of granite, which does not follow the power-law degradation functions proposed by most models.

Acknowledgements The authors would like to express their gratitude to Dr Saurabh Singh for his valuable support during this study. Many thanks also to Mr Aziz Hakimi and Dr Cacin Wong for making their data available to the authors. The latite basalt was kindly supplied by Professor B. Indraratna. This research was funded by the EPSRC grants EP/S026460/1and EP/W000563/1.

Declarations

Conflict of interest The authors declare that they have no conflict of interest regarding their publication in question.

Open Access This article is licensed under a Creative Commons Attribution 4.0 International License, which permits use, sharing, adaptation, distribution and reproduction in any medium or format, as long as you give appropriate credit to the original author(s) and the source, provide a link to the Creative Commons licence, and indicate if changes were made. The images or other third party material in this article are included in the article's Creative Commons licence, unless indicated otherwise in a credit line to the material. If material is not included in the article's Creative Commons licence and your intended use is not permitted by statutory regulation or exceeds the permitted use, you will need to obtain permission directly from the copyright holder. To view a copy of this licence, visit http://creativecommons.org/licenses/by/4.0/.

References

Antonyuk, S., Tomas, J., Heinrich, S., Mörl, L.: Breakage behaviour of spherical granulates by compression. Chem. Engng Sci. **60**(14), 4031–4044 (2005)

Altuhafi, F.N., Baudet, B.A., Coop, M.R.: An investigation of the applicability of contact models to the normal load-deflection behaviour of artificially shaped granite. Acta Geotech. (accepted) (2023). https://doi.org/10.1007/s11440-023-02123-9

Altuhafi, F.N., Coop, M.R.: The small strain stiffness of a railway ballast. Géotechnique (2023). https://doi.org/10.1680/jgeot.22.00356

Bahrami, M., Yovanovich, M.M., Culham, J.R.: A compact model for spherical rough contacts. J. Tribol. **127**(4), 884–889 (2005)

Domede, N., Parent, T., Sellier, A.: Mechanical behaviour of granite. A compilation, analysis and correlation of data from around the world. Eur. J. Environ. Civil Eng. **23**(2), 1–19 (2017)

Goddard, J. D.: Nonlinear elasticity and pressure-dependent wave speeds in granular media. In: Proceedings: Mathematical and Physical Sciences, Vol. 430, No. 1878, pp. 105–31 (1990)

Greenwood, J.A., Tripp, J.H.: The elastic contact of rough spheres. J. Appl. Mech. **34**(1), 153–159 (1967)

Greenwood, J.A., Johnson, K.L., Matsubara, E.: A surface roughness parameter in Hertz contact. Wear **100**(1), 47–57 (1984)

Hertz, H.: Über die Berührung fester elastischer Körper. Journal Für Die Reine Und Angewandte Mathematik **92**, 156–171 (1881)

Indraratna, B., Ionescu, D., Christie, H.D.: Shear behaviour of railway ballast on large-scale triaxial tests. J. Geotech. Geoenviron. Engng. ASCE **124**(5), 439–449 (1998)

Johnson, K.L.: Contact Mechanics. Cambridge University Press, Cambridge (1985)

Mindlin, R.D., Deresiewicz, H.: Elastic spheres in contact under varying oblique force. Trans. ASMEJ. Appl. Mech. **20**, 327–344 (1953)

Nardelli, V., Coop, M.R.: The experimental contact behaviour of natural sands: normal and lateral loading. Géotechnique **69**(8), 672–686 (2019)

Otsubo, M., O'Sulivan, C., Sim, W.W., Ibraim, E.: Quantitative assessment of the influence of surface roughness on soil stiffness. Géotechnique **65**(8), 694–700 (2015)

Paggi, M., Pohrt, R., Popov, V.L.: Partial-slip frictional response of rough surfaces. Sci. Rep. **4**, 5178 (2014). https://doi.org/10.1038/srep05178

Parel, K.S., Paynter, R.J., Nowell, D.: Linear relationship of normal and lateral contact stiffness with load. Proc. R. Soc. A **476**(2020), 0329 (2020)

Persson, B.N.J.: Contact mechanics for randomly rough surfaces. Surf. Sci. Rep. **61**(4), 201–227 (2006)

Pohrt, R., Popov, V.L.: Normal contact stiffness of elastic solids with fractal rough surfaces. Phys. Rev. Lett. **108**(10), 104301 (2012)

Schultz, R.A.: Brittle strength of basaltic rock masses with applications to Venus. J. Geophys. Res. **98**(E6), 10883–10895 (1993)

Scott, P.W., Rollinson, G.K.: Crushed rock aggregates: their mineralogy and textures using automated scanning electron microscopy. In: Hunger, E., Brown, T.J. (eds.), Proceedings of the 18th Extractive Industry Geology Conference, 2014. EIG Conferences, pp. 49–68 (2015)

Tabor, D.: The Hardness of Metals. Oxford University Press, Oxford (1951)

Thornton, C.: Coefficient of reconstitution for collinear collisions of elastic perfectly plastic spheres. J. Appl. Mech. **64**, 383–386 (1997)

Tolomeo, M., McDowell, G.R.: Implementation of real contact behaviour in the DEM modelling of triaxial tests on railway ballast. Powder Technol. **412**, 118021 (2022)

Vu-Quoc, L., Zhang, X.: An accurate and effficient lateral force- displacement model for elastic frictional contact in particles-flow simulations. Mech. Mater. **31**, 235–269 (1999)

Wong, C.P.Y., Coop, M.R.: Development of inter-particle friction in a railway ballast. Géotech. Lett. **10**(4), 535–541 (2020)

Wong, C.P.Y., Coop, M.R.: The contact mechanics of a UK railway ballast. Under review for Géotechnique (2023)

Yang, H., Baudet, B.A., Yao, T.: Characterisation of the surface roughness of sand particles using an advanced fractal approach. Proc. R. Soc. A. **472**, 20160524 (2016)

Yao, T., Baudet, B. A., Lourenço, S. D. N.: Evolution of surface roughness of single sand grains with normal loading, 0 (0), 1–13, Géotechnique, 0 (0), 1–13.(ahead of print) (2021).

Yimsiri, S., Soga, K.: Micromechanics-based stress–strain behaviour of soils at small strains. Géotechnique **50**(5), 559–571 (2000)

Yip, F.C., Venart, J.E.S.: An elastic analysis of the deformation of rough spheres, rough cylinders and rough annuli in contact. J. Phys. D Appl. Phys. **4**(10), 1470 (1971)

Zhao, Y., Maietta, D.M., Chang, L.: An asperity microcontact model incorporating the transition from elastic deformation to fully plastic flow. ASME. J. Tribol. **122**(1), 86–93 (2000)

Publisher's Note Springer Nature remains neutral with regard to jurisdictional claims in published maps and institutional affiliations.